Two-mode long-distance propagation of coseismic ionosphere disturbances

Elvira Astafyeva,[1,2] Kosuke Heki,[1] Vladislav Kiryushkin,[2] Edward Afraimovich,[2] and Sergey Shalimov[3,4]

Received 27 October 2008; revised 24 May 2009; accepted 10 July 2009; published 15 October 2009.

[1] Using GPS total electron content (TEC) measurements, we analyzed ionosphere response to the great Kurile earthquake of 4 October 1994. High spatial resolution of the Japanese dense array of GPS receivers (GEONET) provided us the unique opportunity to observe the evolution of coseismic ionospheric disturbances (CID), which propagated for more than 1800 km away from the epicenter. Plotting a traveltime diagram for the CID and using an ''array processing'' technique within the approximation of a spherical CID wavefront, we observed a phenomenon of CID separation into two modes and we found that characteristics of the CID depend on the distance from the epicenter. The maximum of the CID amplitude was observed at ~500 km from the epicenter. Within the first 600–700 km, the CID propagation velocity was about 1 km/s, which is equal to the sound speed at the height of the ionospheric F-layer. Starting from ~600 to 700 km out from the epicenter, the disturbance seems to divide into two separate perturbations, with each propagating at a different velocity, about 3 km/s for the one and about 600 m/s for the other. Apparently, the TEC response in the far-field of the CID source is a mixture of signals that further ''splits'' into two modes because of the difference in their velocities. Our observations are in good agreement with the results of space-time data processing in the approximation of a spherical wavefront of CID propagation.

Citation: Astafyeva, E., K. Heki, V. Kiryushkin, E. Afraimovich, and S. Shalimov (2009), Two-mode long-distance propagation of coseismic ionosphere disturbances, *J. Geophys. Res.*, *114*, A10307, doi:10.1029/2008JA013853.

1. Introduction

[2] Earthquakes are known to produce infrasonic pressure waves in the atmosphere. Because of the coupling between neutral particles and electrons at ionospheric altitudes, these acoustic and gravity waves induce variations of the ionospheric electron density [*Calais and Minster*, 1998; *Artru et al.*, 2001; *Afraimovich et al.*, 2001a, 2006; *Heki and Ping*, 2005; *Astafyeva and Afraimovich*, 2006].

[3] Coseismic ionosphere disturbances (CID) can be observed both near the epicenter and far from it. However, the physical mechanisms of their generation are different, and therefore their attributes (e.g., the velocity of CID propagation, period, duration, and variations in waveform caused by CID propagation) differ considerably. The source of such CID can be the coseismic vertical crustal movement itself, the consequent propagation of shock-acoustic waves (SAW), surface Rayleigh waves, so-called seismic air waves and tsunamis.

[4] Ionosphere response to SAW propagation can be detected in the vicinity of an earthquake's epicenter 10–15 min after the main shock; CID caused by SAW were found to propagate with a velocity equal to the sound speed (~800–1000 m/s at the height of the ionosphere F-layer). The waveform of the ionosphere response to such a case is usually described as an ''N-type'' wave, consisting of leading and trailing shocks connected by a smooth linear transition region. The waveform arises from nonlinear propagation effects: the amplitude of N waves depends on the magnitude of an earthquake, losses on shock fronts, neutral wind speed, etc. [*Pavlov*, 1986]. The parameters of such CID were well examined by TEC measurements with Global Positioning System (GPS [*Calais and Minster*, 1995, 1998; *Afraimovich et al.*, 2001a, 2006; *Heki and Ping*, 2005; *Heki et al.*, 2006]).

[5] Ionospheric disturbances associated with propagation of surface Rayleigh waves were examined recently using the dense California GPS Networks [*Ducic et al.*, 2003; *Garcia et al.*, 2005] and Doppler techniques [*Artru et al.*, 2004; *Liu et al.*, 2006a]. Following the seismic Rayleigh waves, the certain perturbations in the ionosphere appear to propagate with a velocity about 3.3 km/s. After the 2002 Denali earthquake, TEC was found to be perturbed by about 0.1%, about 0.05 TECU peak to peak [*Ducic et al.*, 2003].

[6] A seismic air wave, appearing because of sudden vertical displacements or tilting of the Earth's surface and propagating horizontally with a velocity about 300 m/s

[1]Department of Natural History Sciences, Hokkaido University, Sapporo, Japan.
[2]Institute of Solar-Terrestrial Physics SB RAS, Irkutsk, Russia.
[3]Institute of Physics of the Earth RAS, Moscow, Russia.
[4]Space Research Institute RAS, Moscow, Russia.

0148-0227/09/2008JA013853$09.00

[*Bolt*, 1964], induces quasiperiodic ionosphere disturbances that can be recorded in the far-field of an earthquake's epicenter [*Astafyeva and Afraimovich*, 2006; *Liu et al.*, 2006a].

[7] A tsunami can be a source of ionosphere disturbances as well [*Liu et al.*, 2006b; *Artru et al.*, 2005]. Such perturbations were reported to be shaped quasiperiodically and to travel with an apparent velocity about 190 m/s, i.e., at the speed of the tsunami wave.

[8] Hence knowing the shape and spatiotemporal characteristics of registered CID we can obtain some information about the source of such disturbances.

[9] Despite numerous papers devoted to the study of features of ionosphere response to large earthquakes, this work is the first report on a new phenomenon of CID separation into two modes during long-distance propagation. High spatial resolution of the Japanese dense array of GPS receivers (GEONET) provided us a unique opportunity to observe the evolution of the observed CID and to study its waveform, propagation characteristics, and source. We compare our observations with modeling results approximating a spherical wavefront of a CID. In conclusion, we discuss possible explanations of the observed phenomena.

2. Methods of Data Processing

[10] GPS ionospheric sounding is known to be one of the most powerful tools for remote sensing of the ionosphere. The dispersive nature of the ionosphere reduces the utility of single frequency GPS measurements. Dual frequency GPS measurements (1.2 and 1.5 GHz) can provide integral information by computing the differential code and carrier phase measurements recorded by ground-based GPS receivers. Methods of TEC calculation have been described in detail in a number of papers [e.g., *Calais and Minster*, 1995; *Afraimovich et al.*, 2001a]. Standard GPS technology provides a means for wave disturbance detection based on phase measurements of slant TEC:

$$I(t) = \frac{1}{40.308} \cdot \frac{f_1^2 f_2^2}{f_1^2 - f_2^2} (L_1\lambda_1 - L_2\lambda_2 + const + nL), \quad (1)$$

where $L_1\lambda_1$ and $L_2\lambda_2$ are additional paths of the radio signal caused by the phase delay in the ionosphere, (m); L_1 and L_2 represent the number of phase rotations at the frequencies f_1 and f_2; λ_1 and λ_2 stand for the corresponding wavelengths, (m); *const* is unknown initial phase path, caused by the unknown number of total phase rotations along the line-of-sight (LOS); and *nL* are errors in determining the phase path; constant 40.308 has the dimension (m^3/s^2). For convenience, TEC is usually measured in TEC units, TECU (1 TECU = 10^{16} m^{-2}). Since TEC is an integral parameter, it is impossible to determine the height of TEC disturbance. However, the main contribution to TEC variations would occur around the height of the maximum ionization. This allows us to consider the ionosphere as a thin layer located at the height h_{max} of the ionosphere F2 layer, and TEC represents a point of intersection of a line-of-sight with the thin layer. We trace propagation of CID by subionospheric point (SIP), a projection of an ionospheric piercing point to the earth's surface. In this paper we assumed h_{max} as 300 km. Low elevation angles tend to enlarge the horizontal extent of the ionospheric region represented by one measurement. Therefore we here used only data with elevations higher than 20 degrees.

[11] To smooth the phase measurement noise and to eliminate variations of the regular ionosphere, as well as the trends introduced by the orbital motion of the satellite, we firstly smooth the initial I(t) series with a time window of 2 min and then remove the linear trend with a window of about 15 min. This works as a band-pass filter to extract variations with period 2–15 min, which is suitable for studying such type of ionosphere disturbances.

[12] The GPS data used in this study come from 30-s rate receivers of the Japanese GPS Earth Observation Network (GEONET, http://terras.gsi.go.jp), which in 1994 had about 100 GPS receivers.

3. Observations: TEC Response to the Earthquake on 4 October 1994

[13] A major earthquake (magnitude 8.1) occurred on 4 October 1994 at 13:23 UT near Shikotan Island, in the subducting Pacific Plate slab, as a high-angle (~50 deg) reverse faulting that resulted in both surface uplift and subsidence of comparable size [*Tsuji et al.*, 1995; *Tanioka et al.*, 1995]. There are two possibilities for the fault geometries that cannot be discriminated with available seismological and geodetic data [*Tsuji et al.*, 1995]. However, the both fault models predict similar vertical coseismic movement patterns characterized by comparable amount of uplift and subsidence. More information about the general characteristics is available on the Web at www.earthquake.usgs.gov and www.eri.u-tokyo.ac.jp/sanchu/Seismo_Note/.

[14] After the earthquake, we observed TEC perturbation in records of only two satellites, PRN06 and PRN20. At this time more satellites were visible, but no signatures of a coseismic TEC perturbation were recorded. Most likely, it is an effect of a strong "aspect" dependence caused by the integral character of a transionospheric sounding. As a first approximation, the transionospheric sounding method is responsive only to ionospheric disturbances with the wave vector **K** perpendicular to the direction **r** of the LOS to the GPS satellite [*Afraimovich et al.*, 2001a].

[15] In Figure 1 we show TEC variations that occurred from the earthquake recorded by satellite 06 and two chains of GPS receivers along the Japanese Islands. Altogether, there are 94 records from the GEONET GPS receivers. Such high spatial resolution allows us to observe the propagation of CID for more than 1800 km. It is obvious from Figure 1 that the amplitude and the shape of variations changed with distance from the epicenter.

[16] At first, ~10–15 minutes after the quake the nearest GPS stations registered a typical N-type TEC perturbation with an amplitude of 0.6 TECU. At a distance 450–500 km, the amplitude of the waves reached the maximum value of 1 TECU and then decreased to 0.2–0.4 TECU in the far-field. A very interesting feature of the propagated perturbation is noticeable from Figure 1. Starting from ~650 to 700 km away from the epicenter the disturbance seems to split into two separate waves which further differ by their dynamic characteristics: one wave propagates farther while

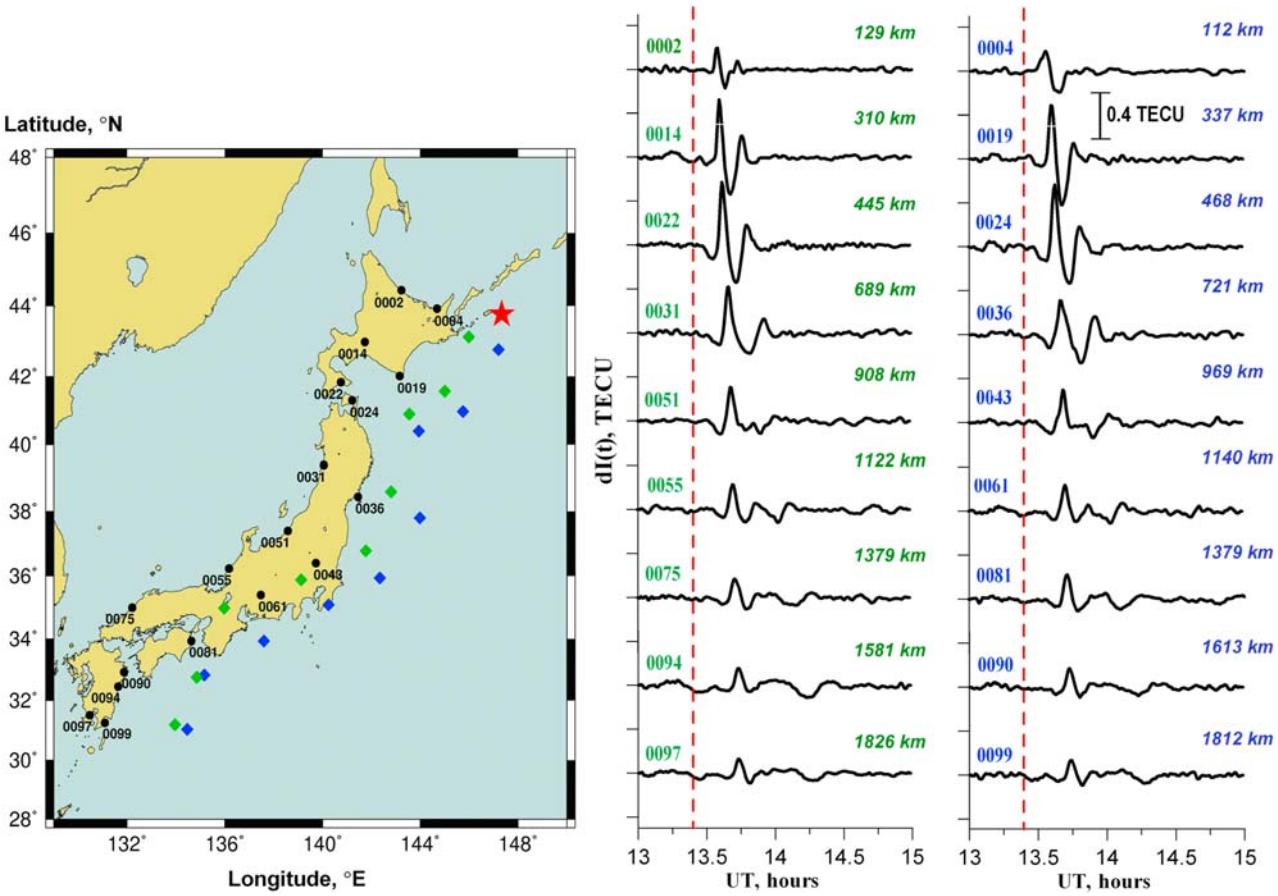

Figure 1. Geometry of (left) GPS measurements and (middle and right) TEC response to the earthquake on 4 October 1994 as recorded by satellite 06. Red star indicates the epicenter of the earthquake. Location of GPS receivers is shown by black dots on the map, and the names of GPS receivers are written next to the dots. Diamonds indicate location of maximums of the TEC response recorded by two chains of GPS receivers (green, GPS stations located on the western coast of the Japanese islands; blue, those located on the eastern coast). Dashed lines on the panels show the moment of the quake. The distance from the epicenter to the point of the TEC maximum value (in km) is written in the panels. Direction of the geomagnetic field at the epicenter of the earthquake is ~57° in inclination and 8° in declination.

the other one fades and becomes almost indiscernible at a distance of about 1800 km.

[17] More detailed information about the evolution of the observed disturbances can be obtained from a traveltime diagram of CID. The diagram is plotted from the arrival times at different subionospheric points and calculating the distance from the source (the center of the uplift) for these points along the great circle path, so that the variously shaped curves align on a certain line, which indicates a linear relationship between traveltimes and focal distances. The diagram for the records of satellite 06 is depicted in Figure 2 (top). The above mentioned splitting of the disturbance and the amplitude variations are easily noticeable in this diagram. Another interesting result concerns the velocity of the observed disturbances that we estimate from the traveltime diagram (the slope of the best fit line of the peaks, arrival times). What we call the initial disturbance propagates with apparent velocity about 990 m/s that equals the sound speed at the height of the ionosphere's F-layer. After the separation we can clearly see components we call "fast" and "slow," with velocities of ~2.7 km/s and ~600 m/s, respectively.

[18] It should be noted that similar results were obtained from the records of satellite 20. Although the geometry of measurements is slightly different, the TEC response registered in the near-field of the epicenter [*Astafyeva and Heki*, 2009], as well as in the far-field, has the same pattern. The traveltime diagram obtained for data of satellite 20 is presented in Figure 2 (bottom). The values of the modes' velocities are close to that of the modes recorded by satellite 06. Velocities are ~1 km/s for the wave in the near-field of the epicenter, ~3 km/s for the fast component and ~660 m/s for the slow component.

4. "Array Processing" Within the Approximation of a Spherical CID Wave Front

[19] In this section, we compute location of the CID source and propagation velocity of the CID from the records of satellite 6. For this purpose we use a technique for an

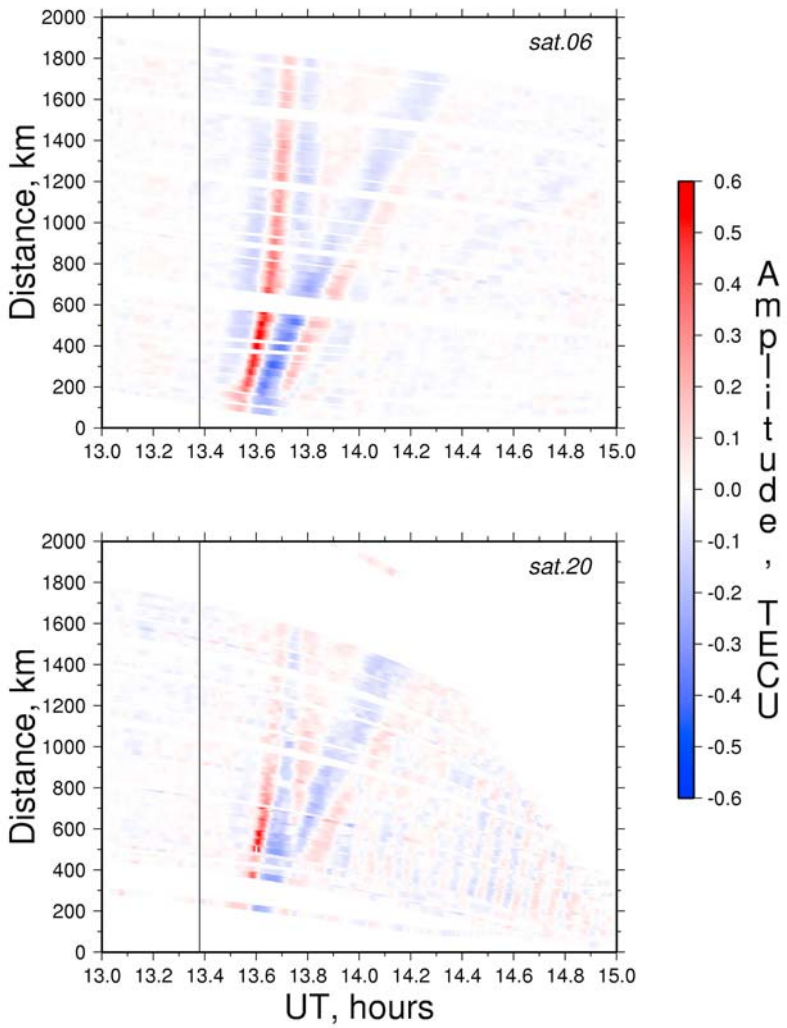

Figure 2. Traveltime diagram for the CID calculated for the records of (top) satellites 06, (bottom) satellite 20, and all available GPS receivers of the GEONET. Distance is measured from the center of the uplift instead of the seismological epicenter. One curve corresponds to one GPS station; colors show CID amplitudes. Time of the quake is indicated by thin line.

"array processing" of TEC series *dI(t)* [*Afraimovich*, 2000; *Afraimovich et al.*, 2001b; *Calais et al.*, 2003]. We consider that the CID propagates from a point source as a spherical wave with constant velocity V (Figure 3 [*Afraimovich et al.*, 2006; *Kiryushkin and Afraimovich*, 2007]). We also propose that the TEC value along GPS LOS is formed in one ionospheric point (IP) at a height $H_{\max}$ = 300 km, so that a set of IPs represents a nonequidistant GPS array. As a result, we know the time (t_i) and the geocentric coordinates (x_i, y_i, z_i) of the CID arrivals in different ionospheric points (registration points), where i = 1, 2 ... M is the number of an IP.

4.1. The Method

[20] Taking a reference point (t_0, x_0, y_0, z_0) and solving the system of equations for the differences of distances ($\Delta\rho_i$) passed by the spherical wave from the point source to the reference point (ρ_0) and to the ith (ρ_i) element of the GPS array, we calculate the time delay $\hat{\tau}$, for which it is necessary to shift each TEC series at the summation. We obtain the slant-stacked series $dI_\Sigma(t)$ as a result of summation with time shifts of all TEC series $dI(t)_i$ of the GPS array.

$$dI_\Sigma = dI_0(t) + \sum_{i=1}^{M} dI_i(t - \hat{\tau}_i) \tag{2}$$

[21] We make these calculations for all possible values of the coordinates (Φ_e, Λ_e) and the height H_e of the point source and the CID propagation velocity V. We determine the "criterion parameter" $C(\Phi_e, \Lambda_e, H_e, V)$ as follows:

$$C = \frac{\sum_{i=1}^{M} \int_{t1}^{t2} \left[dI^m_{\Sigma,i-1}(t) + dI_i\left(t - \tau^m_i(\Phi_e, \Lambda_e, H_e, V)\right)\right]^2 dt}{\sum_{i=1}^{M} \int_{t1}^{t2} \left[dI_{\Sigma,i-1}(t) + dI_i(t - \hat{\tau}_i)\right]^2 dt} \tag{3}$$

[22] This parameter equals the ratio of the total power of phased TEC variations and is estimated at the simulation

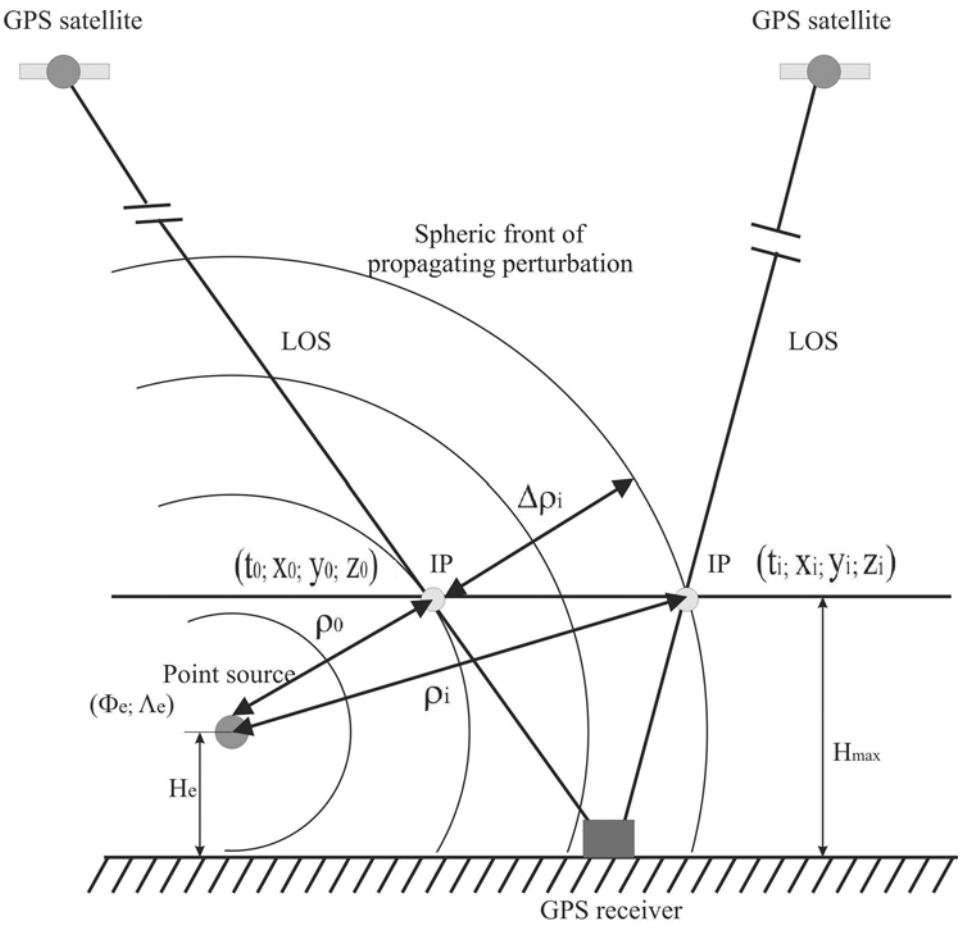

Figure 3. Scheme of the model of spherical perturbation propagated from a point source. (t_i, x_i, y_i, z_i), the time and coordinates of arrivals of a CID in the ith ionospheric points; (t_0, x_0, y_0, z_0), the time and coordinates of reference point; (Φ_e, Λ_e) and H_e, the coordinates and height of the point source; $\Delta\rho_i$, the distance passed by the spherical wave from the point source up to reference (ρ_0) and up to the ith (ρ_i) elements; $H_{\max}$, the height of ionosphere ionization maximum.

stage (numerator) and at the experimental stage (denominator); index e signifies the source, index m means "modeling." Symbols t_1 and t_2 denote the starting and ending moments of integration. The criterion parameter $C(V, \Phi_e, \Lambda_e, H_e)$ defines the degree of the conformity of the modeled disturbance with given parameters (V, Φ_e, Λ_e, H_e) with the space-time dynamics of the observed ionospheric disturbance.

[23] At the experimental processing stage, the output signal $dI_\Sigma(t)$ of the GPS array results from the coherent summation of the TEC series $dI_i(t)$ with the time shifts $\hat{\tau}_i$, so that the correlation coefficient r_i between the ith summable series and the total series in the ith summation iteration $r_i = \int_{t_1}^{t_2} dI_{\Sigma,i-1}(t) dI_i(t - \tau_i) dt$ reaches its maximum value. This is the necessary condition for the maximization of the resultant total energy of the signal [*Kiryushkin and Afraimovich*, 2007]. Primarily, the summation is applied to a certain TEC series $dI_0(t)$ that is chosen as the central element of the array and for which the mean coefficient of the correlation with all other series $dI_i(t)$ is of the maximum value. The output signal of the GPS array at the simulation stage $dI_\Sigma^m(t)$ results from the summation of all TEC series $dI_i(t)$ with the time shifts τ_i^m calculated within the approximation of the spherical disturbance propagating with the given velocity V from the point source of the given coordinates (Φ_e, Λ_e) and the height H_e. In this case we minimize the difference $(t_i - t_0) - \frac{\Delta\rho_i}{V}$, where $\Delta\rho_i = \rho_i - \rho_0$ is the difference of distances traveled by the modeled ionospheric disturbance from the given source to the central (at t_0) and the ith (at t_i) elements of the GPS array. During the processing, we find the maximum value of the amplitude $dI_{\max,i}$, the time $t_{\max,i}$ corresponding to the $dI_{\max,i}$ as well as the distance between a registration point and the source D_i along the great circle arc. The CID velocity in each registration point is defined as follows:

$$V_i = \frac{D_i - D_0}{\tau_i^m}, \tag{4}$$

where D_0 is the distance from the source to the point of registration of the "reference" TEC response that corresponds to the central element of the array; D_i is the distance between the source and the ith registration point; $\tau_i^m = t_{\max,i} - t_{\max,0}$ is the time delay between the response registration in the reference TEC series $dI_0(t)$ and in the ith TEC series $dI_i(t)$.

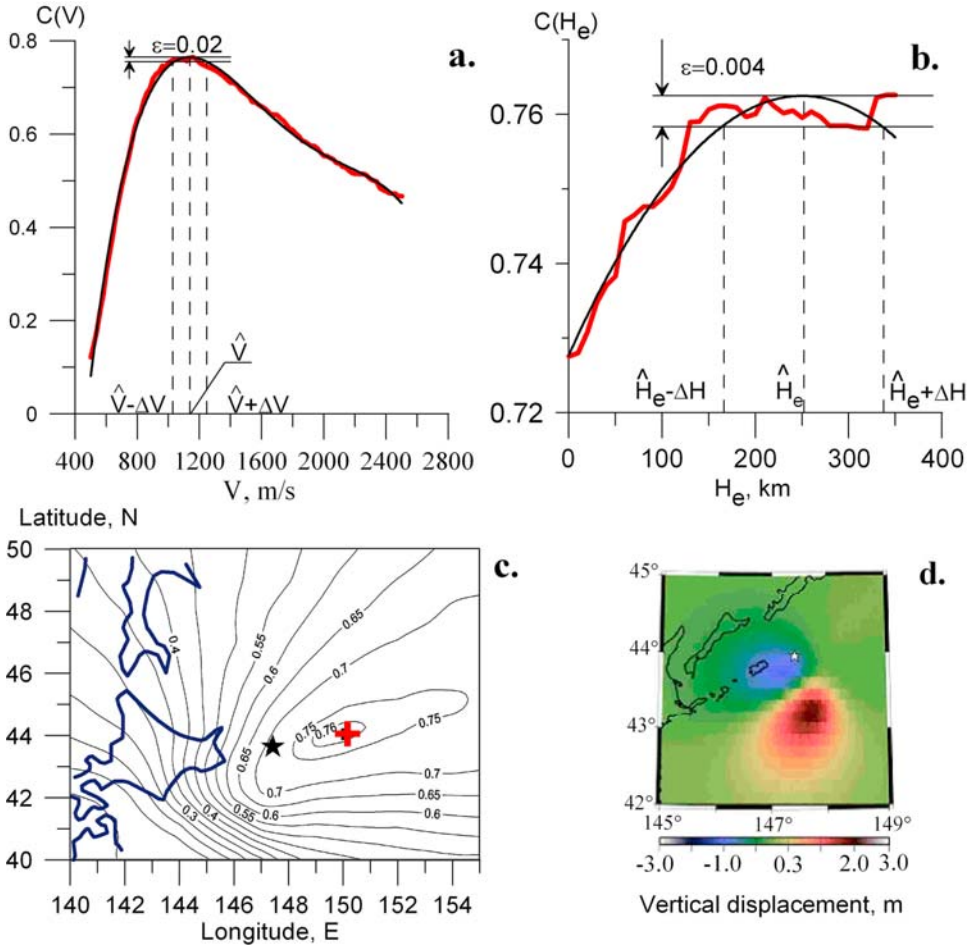

Figure 4. Results of the space-time processing in the approximation of the spherical wave propagation (near-field region). Dependencies of the parameter C on (a) CID velocity $\hat{V}$ and (b) the CID source height $\hat{H}_e$. Red and black colors correspond to the modeling and approximation dependencies, respectively. Vertical broken lines show the accuracy of determination of the CID velocity and the source height, caused by the accuracy of calculation of the maximum of parameter C. (c) Positions of the seismological epicenter (asterisk) and calculated CID source (cross), corresponding the $C(\hat{\Phi}_e, \hat{\Lambda}_e)$ maximum. (d) Vertical coseismic crustal movements due to the earthquake on 4 October 1994 calculated using the model by *Okada* [1992].

[24] "Switching-on time of the source" is calculated from the computed values of the CID's velocity, coordinates of the CID source, as well as coordinates and time of the disturbance registered by the central element of the GPS array:

$$t_e = t_0 - \frac{\sqrt{(x_0 - \hat{x}_e)^2 + (y_0 - \hat{y}_e)^2 + (z_0 - \hat{z}_e)^2}}{\hat{V}} \qquad (5)$$

where $(\hat{x}_e, \hat{y}_e, \hat{z}_e)$ are the estimated values of the geocentric coordinates of the CID's source, which are obtained through the standard transformations of the estimates $(\hat{\Phi}_e, \hat{\Lambda}_e, \hat{H}_e)$; (x_0, y_0, z_0) are the coordinates of the central element of the GPS array.

4.2. Near-Field Region

[25] First we bounded the GPS array by the stations located in the near-field region of the seismic epicenter (<700 km), before the separation into the fast and slow components. Figures 4a and 4b present the dependences of the criterion parameter C on the velocity $C(V)$ and the source height $C(H_e)$, including an error (thin black curves). Thick gray curves show the approximation curves of these dependences. The maximum C values correspond to the propagation velocity of V = 1150 ± 100 m/s and to the height of the ionospheric disturbance source of $\hat{H}_e$ = 250 ± 80 km.

[26] As seen from Figure 4c, the maximum of the two-dimensional dependence $C(\Phi_e, \Lambda_e)$ corresponds to the source with geographical coordinates 44°N, 149.8°E. The obtained dependence of the criterion parameter C on the coordinates $C(\Phi_e, \Lambda_e)$ shows that the position of the calculated point source of the observed CID (shown by cross) was located ~100 km northeast from the seismological epicenter (shown by asterisk). Such a distinction can be explained by (1) the fact that the seismological epicenter might not coincide with a point of maximum acoustic energy released at the quake and (2) possible influence of the neutral winds on the propagation of the perturbation

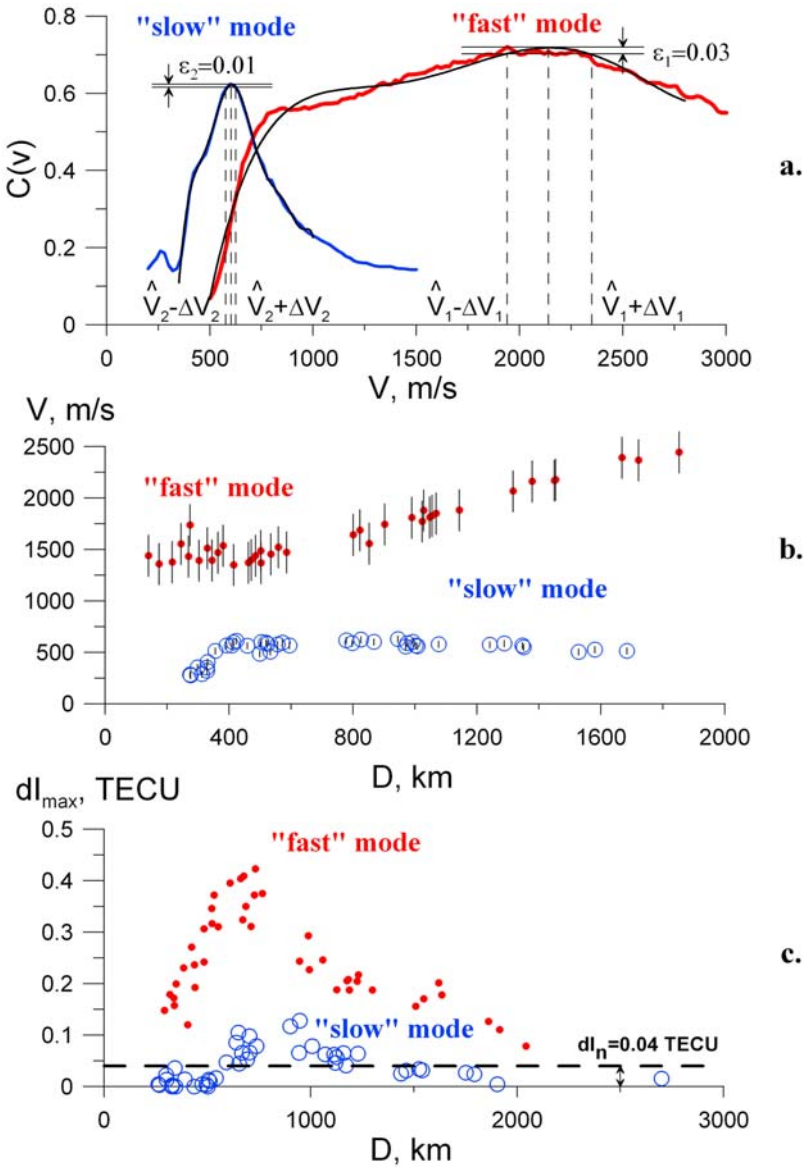

Figure 5. Results of the space-time processing in the approximation of the spherical wave propagation (far-field region): red and blue colors correspond to the "fast" and "slow" modes, respectively. (a) Dependence of the parameter $C(V)$; vertical broken lines mark the limits of accuracy of CID velocity determination caused by the accuracy of parameter C maximum calculation. (b) CID velocity as dependent on distance D from the source; (c) Dependence of maximum value of CID amplitude $dI_{max}(D)$ on distance D.

while reaching the ionospheric heights. In the first case, the vertical crustal displacements that occurred due to the earthquake (Figure 4d), create an uplift area that might serve as the main site of the acoustic energy emission. However, in our case the uplift area does not coincide with the location of the point CID source (Figures 4c and 4d). The estimated location of the CID source corresponds to the time 13.53 UT of the CID source's switching-on, which is ~9 min after the quake. This result agrees with the conception that the source of an ionosphere disturbance is not an earthquake's epicenter itself, but an area between 120 and 350 km of height where propagating upward acoustic waves overturn due to strong nonlinear effects [*Afraimovich et al.*, 2006; *Kiryushkin and Afraimovich*, 2007].

4.3. Far-Field Region

[27] In order to analyze characteristics of the splitted modes, we selected by time the TEC series with the data corresponding to the both components. Thus the data series from 13.38 UT to 13.74 UT correspond to the fast wave, and the period from 13.75 UT to 15.3 UT to the slow wave. We took the position of the CID source at a height of 250 km over the seismic epicenter and carried out the space-time processing for the fast and slow modes of the disturbance, estimating the propagation velocity of each wave. For this purpose we used the entire GPS array, but the TEC series were limited in time: $t \leq 13.75$ UT for the fast mode and $t \geq 13.75$ UT for the slow one. The dependence of the propagation velocity criterion parameter $C(V)$ for the

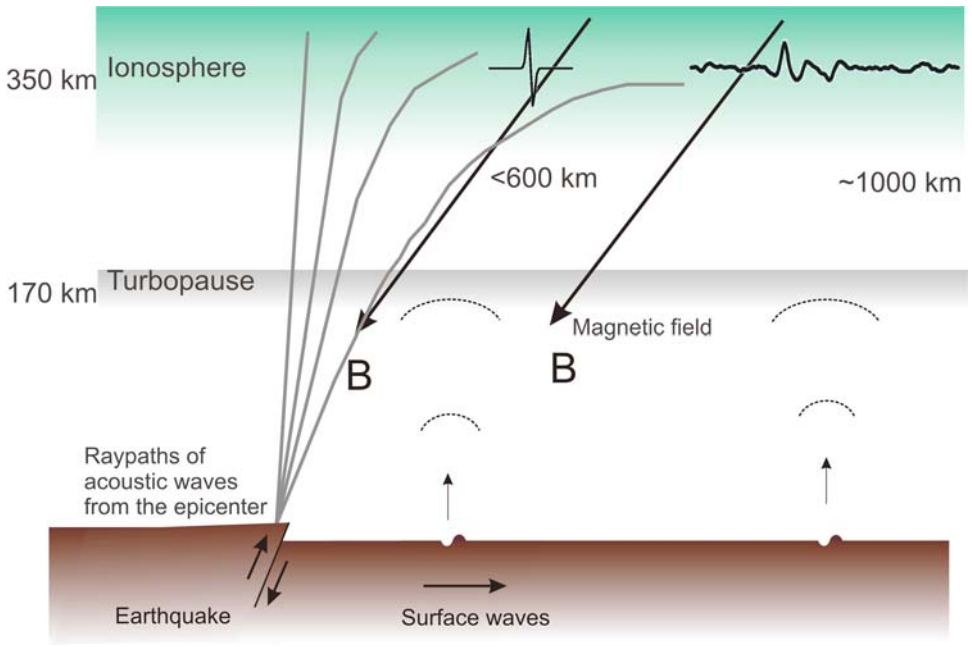

Figure 6. Scheme for the proposed explanations of the observations: superposition of acoustic waves induced by the Rayleigh surface waves and by the quake itself. Influence of geomagnetic field becomes important after ~150 km of altitude.

separated waves with the confidence intervals of the estimates is presented in Figure 5a. Determining the disturbance velocity in each registration point, we obtained the dependence of the velocity of each CID mode on distance $V(D)$ (Figure 5b).

[28] As seen from Figure 5a, the two separated perturbations can be characterized by different velocity values. The velocity of the "fast" perturbation essentially exceeds the sound speed and increases with distance from the source, from 1.5 km/s at a distance of 800 km to 2.5 km/s at a distance of 1800 km. These values differ from those we calculated from the traveltime diagrams presented in Figure 2. Such a difference can be explained by the approximations we used within this method, e.g., a spherical wavefront and the constant propagation velocity that was calculated from the delay in response between the point source and a registration point. The "slow" perturbation propagates with a velocity less than the sound speed and further slows down to 400 m/s at a distance of 1800 km (Figure 5b).

[29] Figure 5c presents the dependence of the maximum value of CID amplitude dI_{max} (D) on distance D for the fast (dots) and slow (circles) modes. The horizontal dashed line marks the level of TEC noise of ~0.04 TECU. Dependence dI_{max} (D) shows that the maximum of amplitude is reached at distance about 500 km from the epicenter. Then, at ~1800 km away from the epicenter the CID blurred.

5. Discussions and Conclusion

[30] Use of GPS TEC measurements by the dense array of GPS receivers GEONET provided us the unique opportunity to record long-distance propagation of ionosphere disturbances associated with the great Kurile earthquake of 4 October 1994. A phenomenon of the CID separation into two modes was observed.

[31] Within the first 600–700 km, the CID is N-shaped and propagates with the velocity of about of 1 km/s, that is equal to the sound speed at the height of the ionosphere F-layer. Starting from ~600 to 700 km out of the epicenter, the disturbance seems to divide into two perturbations which propagate with different velocities, one at about 3 km/s and the other at about 600 m/s. Apparently, the TEC response in the near-field of the CID source is a mixture of signals that are further observable as two separate modes because of the difference in their velocities. With regard to the possible explanation of our observations, we suggest that the fast and slow components, most likely, were triggered by the Rayleigh surface waves and by the quake itself (Figure 6). Namely, the two modes are the perturbations of electron density by acoustic waves launched by Rayleigh surface wave and by the vertical displacements of the ground due to the earthquake. Then, in the near-field that is comparable with the wavelength of the Rayleigh surface wave, the components are indiscernible, but after 600–700 km both modes become apparent in the TEC data series. The separated "fast" mode propagates with apparent mean velocity of about of 3 km/s that is close to the velocity of Rayleigh surface waves. The amplitude and the shape of the fast mode remained practically unchangeable during the next 1500 km while we were able to perform TEC measurements. This is an additional evidence for the fast perturbation to be caused by a travelling source (in contrast to a point source) that we attributed to propagating Rayleigh waves. Other interesting feature of the fast mode is its acceleration with distance from the epicenter (Figures 2 and 5). This acceleration is, most likely, seeming and appears due to the approximations used in the methods of data processing, as mentioned in p. 4.3. Apart from that, the Rayleigh surface waves are known to be better pronounced in the far-field of the source because of their long wave-

length (hundreds of km), which can lead to a seeming effect of the CID acceleration after ~700 km of distance. At the same time, the slow component slowed down and finally faded out at ~1800 km from the epicenter. Considering that this component corresponds to acoustic wave launched by the quake itself, it gives us information about the radius of a possible observation of acoustic waves, i.e., ~1800 km away from the epicenter of an earthquake. Note that the slow component appears to be somewhat negative in phase at distance ~1000 km, and this can be explained by the known feature of propagating acoustic waves: the high-frequency components attenuate faster than the low-frequency ones.

[32] The observed difference in the shape of the separated modes can be also explained by taking into account that infrasound waves propagate in the presence of a geomagnetic field (Figure 6). Then, considering that the observed modes represent acoustic waves induced by the Rayleigh surface waves and those launched by the quake, we presume that the slow component of the ionospheric response is stipulated by the N-type acoustic wave that propagates from the epicenter, reaching and penetrating the ionosphere at different angles in accordance with ray-tracing paths. In this case the CID's horizontal traveling is apparent. The observed spreading of the positive and negative phases of the slow ionospheric response can be attributed to the different speed of propagation for the positive and negative phases of the initial atmospheric disturbance (i.e., the compression-rarefaction phases of the acoustic N wave). At some altitude where the magnetic pressure dominates the thermal pressure (at about 160–170 km) an acoustic wave propagating upward from the ground to ionospheric level transforms into the fast magnetic sound which is the same wave mode as the nonmagnetic sound [*Ostrovsky*, 2008]. In cases in which magnetic forces dominate the displacement of plasma becomes mostly in direction across the magnetic field due to "frozen-in" condition. This gives compression and rarefaction phases of the ionospheric disturbance. Then the observed maximum of acoustic wave amplitude at a horizontal distance 500 km can be explained by the interplaying of the damping with distance and influence of the geomagnetic field inclination in the point of penetration.

[33] It should be noted, however, that before acoustic waves reach the ionosphere heights, they evolve due to nonlinear effects provided by the atmospheric medium. This primarily concerns their transformation into shock-acoustic waves, upon their propagation in a viscous medium with decreasing density (i.e., upward in the atmosphere), then the leading edge of the wavefront steepens and jumps of density, pressure, etc. appear. Apart from that, due to the viscosity increases after ~100 km of height, the dissipation processes strengthen as well, so dynamical energy is converted into heat [e.g., *Blanc*, 1985]. According to *Hines* [1965], this heat can be of a very high value, so that there was proposed a hypothesis that such heated area can be a source of a sort of "secondary" disturbance, which we actually register in the ionosphere [*Afraimovich et al.*, 2006]. In this case, the source of the ionosphere disturbance is located in the atmosphere somewhat higher 110–120 km (after the turbopause) and above the earthquake's epicenter (Figure 3). Previous estimations of parameters of CID source within the approximation of a spherical wavefront for the Tokachi-oki earthquake of 25 September 2003 and for the Sumatra earthquake on 4 June 2000 showed that the CID source was located at the height of 260–350 km [*Afraimovich et al.*, 2006]. The switching-on time of the source was ~490–550 s after the main quake, that corresponds to the time that is necessary for acoustic waves to reach the height of the source. However, for better understanding of the formation mechanism for coseismic ionosphere disturbances, modeling and further experimental investigations of the whole process are necessary.

[34] **Acknowledgments.** The work is supported by the Japanese Society for the Promotion of Science (JSPS), by the Russian Foundation for Basic Research (RFBR, grant 07-05-00127), by the SB RAS and FEB RAS collaboration project N 3.24, and by the Interdisciplinary integral project of SB RAS N 56 "Seismoionospheric and seismoelectromagnetic processes in Baikal Rift Zone."

[35] Amitava Bhattacharjee thanks J.Y. Liu and another reviewer for their assistance in evaluating this paper.

References

Afraimovich, E. L. (2000), GPS global detection of the ionospheric response to solar flares, *Radio Sci.*, *35*(6), 1417–1424.

Afraimovich, E. L., N. P. Perevalova, A. V. Plotnikov, and A. M. Uralov (2001a), The shock-acoustic waves generated by the earthquakes, *Ann. Geophys.*, *19*(4), 395–409.

Afraimovich, E. L., V. V. Chernukhov, and V. V. Kiryushkin (2001b), Spatial-temporal characteristics of the ionospheric disturbances induced by shock-acoustic waves due to rocket launching, *J. Commun. Technol. Electronics*, *46*(11), 1199–1206.

Afraimovich, E. L., E. I. Astafieva, and V. V. Kirushkin (2006), Localization of the source of ionospheric disturbance generated during an earthquake, *Int. J. Geomagn. Aeron.*, *6*(2), GI2002, doi:10.1029/2004GI000092.

Artru, J., P. Lognonne, and E. Blanc (2001), Normal modes modelling of post-seismic ionospheric oscillations, *Geophys. Res. Lett.*, *28*(4), 697–700.

Artru, J., T. Farges, and P. Lognonne (2004), Acoustic waves generated from seismic surface waves: Propagation properties determined from Doppler sounding observations and normal-mode modelling, *Geophys. J. Int.*, *158*(6), 1067–1077.

Artru, J., P. Lognonné, G. Occhipinti, F. Crespon, R. Garcia, E. Jeansou, and M. Murakami (2005), Tsunami detection in the ionosphere, *Space Res. Today*, *163*, 23–27.

Astafyeva, E. I., and E. L. Afraimovich (2006), Long-distance propagation of traveling ionospheric disturbances caused by the great Sumatra-Andaman earthquake on 26 December 2004, *Earth Planets Space*, *58*(8), 1025–1031.

Astafyeva, E., and K. Heki (2009), Dependence of waveform of near-field coseismic ionospheric disturbances on focal mechanisms, *Earth Planets Space*, *16*, 939–943.

Blanc, E. (1985), Observations in the upper atmosphere of infrasonic waves from naturalor artificial sources: A summary, *Ann. Geophys.*, *3*(6), 673–688.

Bolt, B. A. (1964), Seismic air waves from the great 1964 Alaskan earthquake, *Nature*, *202*, 1094–1095.

Calais, E., and J. B. Minster (1995), GPS detection of ionospheric perturbations following the January 17, 1994, Northridge earthquake, *Geophys. Res. Lett.*, *22*(9), 1045–1048.

Calais, E., and J. B. Minster (1998), GPS, earthquakes, the ionosphere, and the Space Shuttle, *Phys. Earth Planet. Inter.*, *105*, 167–181.

Calais, E., J. S. Haase, and J. B. Minster (2003), Detection of ionospheric perturbations using dense GPS arrays in Southern California, *Geophys. Res. Lett.*, *30*(12), 1628, doi:10.1029/2003GL017708.

Ducic, V., J. Artru, and P. Lognonne (2003), Ionospheric remote sensing of the Denali earthquake Rayleigh surface waves, *Geophys. Res. Lett.*, *30*(18), 1951, doi:10.1029/2003GL017812.

Garcia, R., F. Crespon, V. Ducic, and P. Lognonne (2005), Three-dimensional ionospheric tomography of post-seismic pertubations produced by the Denali earthquake from GPS data, *Geophys. J. Int.*, *163*, 1049–1064.

Heki, K., and J. Ping (2005), Directivity and apparent velocity of the coseismic ionospheric disturbances observed with a dense GPS array, *Earth Planet Sci. Lett.*, *236*, 845–855.

Heki, K., Y. Otsuka, N. Choosakul, N. Hemmakorn, T. Komolmis, and T. Maruyama (2006), Detection of ruptures of Andaman fault segments in the 2004 great Sumatra earthquake with coseismic ionospheric disturbances, *J. Geophys. Res.*, *111*, B09313, doi:10.1029/2005JB004202.

Hines, C. O. (1965), Dynamical heating of the upper atmosphere, *J. Geophys. Res.*, *70*(1), 177–183.

Kiryushkin, V. V., and E. L. Afraimovich (2007), Determining the parameters of ionospheric perturbation caused by earthquakes using the quasi-optimum algorithm of spatiotemporal processing of TEC measurements, *Earth Planets Space*, *59*, 267–278.

Liu, J. Y., Y. B. Tsai, S. W. Chen, C. P. Lee, Y. C. Chen, H. Y. Yen, W. Y. Chang, and C. Liu (2006a), Giant ionospheric disturbances excited by the M9.3 Sumatra earthquake on 26 December 2004, *Geophys. Res. Lett.*, *33*, L02103, doi:10.1029/2005GL023963.

Liu, J.-Y., Y.-B. Tsai, K.-F. Ma, Y.-I. Chen, H.-F. Tsai, C.-H. Lin, M. Kamogawa, and C.-P. Lee (2006b), Ionospheric GPS total electron content (TEC) disturbances triggered by the 26 December 2004 Indian Ocean tsunami, *J. Geophys. Res.*, *111*, A05303, doi:10.1029/2005JA011200.

Okada, Y. (1992), Internal deformation due to shear and tensile faults in a half-space, *Bull. Seismol. Soc. Am.*, *82*, 1018–1040.

Ostrovsky, L. A. (2008), Ionospheric effects of ground motion: The roles of magnetic field and nonlinearity, *J. Atmos. Sol. Terr. Phys.*, *70*, 1273–1280.

Pavlov, V. A. (1986), The acoustic pulse above the epicenter of an earthquake, *Geomagn. Aeron.*, *26*, 678–683.

Tanioka, Y., L. Ruff, and K. Satake (1995), The great Kurile earthquake of October 4, 1994 tore the slab, *Geophys. Res. Lett.*, *22*(13), 1661–1664.

Tsuji, H., Y. Hatanaka, T. Sagiya, and M. Hashimoto (1995), Coseismic crustal deformation from the 1994 Hokkaido-Toho-Oki earthquake monitored by a nationwide continuous GPS array in Japan, *Geophys. Res. Lett.*, *22*(13), 1669–1672.

E. Afraimovich and V. Kiryushkin, Institute of Solar-Terrestrial Physics SB RAS, Lermontova Str., 126A, Irkutsk 664033, Russia.

E. Astafyeva and K. Heki, Department of Natural History Sciences, Hokkaido University, Kita-ku N10 W8, Sapporo 060-0810, Japan. (elliada@mail.sci.hokudai.ac.jp)

S. Shalimov, Institute of Physics of the Earth RAS, Bol'shaya Gruzinskaya str., 10, 123995 Moscow, Russia.